

1 **Tropopause Evolution in a Rapidly Intensifying Tropical Cyclone: A Static**
2 **Stability Budget Analysis in an Idealized, Axisymmetric Framework**

3 Patrick Duran* and John Molinari

4 *University at Albany, State University of New York, Albany, NY*

5 **Corresponding author address:* Department of Atmospheric and Environmental Sciences, Univer-
6 sity at Albany, State University of New York, 1400 Washington Avenue, Albany, NY.

7 E-mail: pduran2008@gmail.com

ABSTRACT

8 Large changes in tropopause-layer static stability are examined during the
9 rapid intensification (RI) of a tropical cyclone (TC) in an idealized, axisym-
10 metric simulation. Over the eye, static stability near the tropopause decreases
11 and the cold-point tropopause height rises by up to 4 km at the storm center.
12 Outside of the eye, static stability increases considerably just above the cold-
13 point tropopause, and the tropopause remains near its initial level.

14 A budget analysis reveals that the advection term, which includes differen-
15 tial advection of potential temperature and direct advection of static stability,
16 is important throughout the upper troposphere and lower stratosphere. Within
17 the eye, differential advection plays a particularly important role in destabi-
18 lizing the layer near and above the cold-point tropopause. Outside of the eye,
19 the upper-tropospheric outflow layer exports high potential temperature (θ)
20 air from the eyewall to large radii in the upper troposphere. This increase in
21 θ forces stabilization below the outflow jet and destabilization above. Vertical
22 wind shear above and below the outflow maximum induces vertical gradi-
23 ents of turbulence, which also modify the vertical stability profile. Mean-
24 while, radiative cooling tendencies at the top of the cirrus canopy generally
25 act to destabilize the upper troposphere and stabilize the lower stratosphere.
26 These turbulent and radiative processes combine to play an important role in
27 the development of the strong stable layer immediately above the cold-point
28 tropopause during RI.

29 **1. Introduction**

30 Using a high-resolution dropsonde dataset collected during the Tropical Cyclone Intensity Ex-
31 periment (TCI; Doyle et al. 2017), Duran and Molinari (2018) observed dramatic changes in
32 tropopause structure during the rapid intensification (RI) of Hurricane Patricia (2015). The goal of
33 the present paper is to analyze the processes that might have produced the upper-tropospheric and
34 lower-stratospheric fluctuations observed in Patricia using an idealized axisymmetric simulation.

35 After undergoing a remarkably rapid intensification (RI), Hurricane Patricia (2015) attained the
36 strongest wind speed ever recorded in a tropical cyclone (TC) (Kimberlain et al. 2016; Rogers et al.
37 2017). TCI dropsonde observations collected during this RI period revealed dramatic changes in
38 the cold-point tropopause height and upper-level static stability (Duran and Molinari 2018). In
39 particular, when Patricia was at tropical storm intensity shortly before RI commenced, a strong in-
40 version layer existed just above the cold-point tropopause (see their Fig. 4a). During the first half
41 of the RI period, this inversion layer weakened throughout Patricia’s inner core, with the weaken-
42 ing most pronounced over the developing eye. By the time the storm reached its maximum best-
43 track intensity of 95 m s^{-1} , the inversion layer over the eye had disappeared almost completely (see
44 their Fig. 4d), which was accompanied by a greater than 1-km increase in the tropopause height.
45 Meanwhile over the eyewall region, the static stability increased and the tropopause remained near
46 its initial level.

47 Despite the importance of tropopause-layer thermodynamics in theoretical models of hurri-
48 canes (Emanuel and Rotunno 2011; Emanuel 2012), most observational studies of the upper-
49 tropospheric structure of TCs are decades old¹. Recently, however, Komaromi and Doyle (2017)
50 found that stronger TCs tended to have a higher and warmer tropopause over their inner core than
51 weaker TCs. Their results are consistent with the evolution observed over the inner core of Hur-

¹ An in-depth review of these papers can be found in Duran and Molinari (2018).

52 ricane Patricia, in which the tropopause height increased and the tropopause temperature warmed
53 throughout RI (Duran and Molinari 2018).

54 An idealized simulation of a TC analyzed by Ohno and Satoh (2015) suggested that the devel-
55 opment of an upper-level warm core near the 13-km level acted to decrease the static stability near
56 the tropopause within the eye. During the early stage of development in their simulation, large
57 static stability existed above 16 km at all radii (their Fig. 9c). However, after the storm's inten-
58 sification, the static stability within the eye above 16 km was markedly smaller (their Fig. 10c).
59 Although the mechanisms that might drive this static stability evolution have not been examined
60 explicitly, it might be related to the development of an upper-tropospheric warm core within the
61 eye.

62 Stern and Zhang (2013) described the development of the TC warm core using a potential tem-
63 perature (θ) budget analysis. Although the warm anomaly in their simulation maximized in the
64 mid-levels, they noted that a secondary warming maximum also existed in the 12-14-km layer.
65 Radial and vertical advection both played important roles in this warm core development through-
66 out RI, and subgrid-scale diffusion became particularly important during the later stage of RI.
67 The warming of the upper troposphere by these advective and diffusive processes could decrease
68 the vertical θ gradient, thereby contributing to a decrease in static stability near the tropopause
69 within the eye.

70 Outside of the eye, in the presence of cirrus clouds, vertical gradients of radiative heating also
71 can modify the tropopause-layer static stability. Bu et al. (2014) noted the existence of a shallow
72 region of diurnal-mean net radiative cooling at the top of the TC cirrus canopy (see their Figs. 5,
73 11). This shallow region of cooling could act to destabilize the layer just below the top of the cirrus
74 canopy and stabilize the layer immediately above. If the top of the cirrus canopy lies close to the

75 tropopause, these radiative processes could contribute to a stabilization of the lower stratosphere,
76 as was observed in Hurricane Patricia.

77 To our knowledge, the only paper that has examined explicitly the static stability evolution
78 in a modeled TC is Kepert et al. (2016), but their analysis was limited to the boundary layer.
79 The analysis herein is based upon that of Stern and Zhang (2013), except using a static stability
80 budget similar to that of Kepert et al. (2016), with a focus on the upper-tropospheric and lower-
81 stratospheric evolution during RI.

82 **2. Model Setup**

83 The numerical simulations were performed using version 19.4 of Cloud Model 1 (CM1) de-
84 scribed in Bryan and Rotunno (2009). The equations of motion were integrated on a 3000-km-
85 wide, 30-km-deep axisymmetric grid with 1-km horizontal and 250-m vertical grid spacing. The
86 computations were performed on an f -plane at 15°N latitude, over a sea surface with constant
87 temperature of 30.5°C, which is based on that analyzed near Hurricane Patricia (2015; Kimberlain
88 et al. 2016). Horizontal turbulence was parameterized using the Smagorinsky scheme described
89 in Bryan and Rotunno (2009, pg. 1773), with a prescribed mixing length that varied linearly from
90 100 m at a surface pressure of 1015 hPa to 1000 m at a surface pressure of 900 hPa. Vertical
91 turbulence was parameterized using the formulation of Markowski and Bryan (2016, their Eq.
92 6), using an asymptotic vertical mixing length of 100 m, which is the default setup for hurricane
93 simulations in CM1. A Rayleigh damping layer was applied outside of the 2900-km radius and
94 above the 25-km level to prevent spurious gravity wave reflection at the model boundaries. Mi-
95 crophysical processes were parameterized using the Thompson et al. (2004) scheme, and radiative
96 heating tendencies were computed every two minutes using the Rapid Radiative Transfer Model
97 for GCMs (RRTMG) longwave and shortwave schemes (Iacono et al. 2008). The initial temper-

ature and humidity field was horizontally homogeneous and determined by averaging all Climate Forecast System Reanalysis (CFSR) grid points within 100 km of Patricia's center of circulation at 18 UTC 21 October 2015. The vortex described in Rotunno and Emanuel (1987, their Eq. 37) was used to initialize the wind field, setting all parameters equal to the values used therein.

Although hurricanes simulated in an axisymmetric framework tend to be more intense than those observed in nature, the intensity evolution of this simulation matches reasonably well with that observed in Hurricane Patricia. After an initial spin-up period of about 20 hours, the modeled storm (Fig. 1, blue lines) began an RI period that lasted approximately 18 hours. After this RI, the storm continued to intensify more slowly until the maximum 10-m wind speed reached 89 m s^{-1} and the sea-level pressure reached its minimum of 846 hPa 81 hours into the simulation. Hurricane Patricia (red stars) exhibited a similar intensity evolution prior to its landfall, with an RI period leading to a maximum 10-m wind speed of 95 m s^{-1} and a minimum sea-level pressure of 872 hPa.

3. Budget Computation

The static stability can be expressed as the squared Brunt-Väisälä frequency:

$$N_m^2 = \frac{g}{T} \left(\frac{\partial T}{\partial z} + \Gamma_m \right) \left(1 + \frac{T}{R_d/R_v + q_s} \frac{\partial q_s}{\partial T} \right) - \frac{g}{1 + q_t} \frac{\partial q_t}{\partial z}, \quad (1)$$

where g is gravitational acceleration, T is temperature, R_d and R_v are the gas constants of dry air and water vapor, respectively, q_s is the saturation mixing ratio, q_t is the total condensate mixing ratio, and Γ_m is the moist-adiabatic lapse rate:

$$\Gamma_m = g(1 + q_t) \left(\frac{1 + L_v q_s / R_d T}{c_{pm} + L_v \partial q_s / \partial T} \right), \quad (2)$$

where L_v is the latent heat of vaporization and c_{pm} is the specific heat of moist air at constant pressure. In the tropopause layer, q_s , q_t , $\partial q_s / \partial T$, and $\partial q_t / \partial z$ approach zero. In this limiting case,

Eq. 1 reduces to:

$$N^2 = \frac{g}{\theta} \frac{\partial \theta}{\partial z}, \quad (3)$$

where θ is the potential temperature.

To compute N^2 , CM1 uses Eq. 1 in saturated environments and Eq. 3 in sub-saturated environments. For simplicity, however, only Eq. 3 will be employed for the budget computations throughout the entire domain².

Taking the time derivative of Eq. 3 yields the static stability tendency:

$$\frac{\partial N^2}{\partial t} = \frac{g}{\theta} \frac{\partial}{\partial z} \frac{\partial \theta}{\partial t} - \frac{g}{\theta^2} \frac{\partial \theta}{\partial z} \frac{\partial \theta}{\partial t}, \quad (4)$$

where the potential temperature tendency, $\partial \theta / \partial t$, can be written, following Bryan (cited 2018):

$$\frac{\partial \theta}{\partial t} = -u \frac{\partial \theta}{\partial r} - w \frac{\partial \theta}{\partial z} + HTURB + VTURB + MP + RAD + DISS \quad (5)$$

Each term on the right-hand side of Eq. 5 represents a θ budget variable, each of which is output directly by the model every minute.

The first term on the right-hand side of Eq. 4 is larger than the second term throughout most of the tropopause layer (not shown). Consequently, the contribution of each of the terms in Eq. 5 to the N^2 tendency can be interpreted in light of a vertical gradient of each term.

Taking the vertical gradient of the first two terms on the right-hand side of Eq. 5 yields the time tendency of the vertical θ gradient due to horizontal and vertical advection³:

$$\left(\frac{\partial}{\partial t} \frac{\partial \theta}{\partial z} \right)_{adv} = -u \frac{\partial}{\partial r} \frac{\partial \theta}{\partial z} - w \frac{\partial}{\partial z} \frac{\partial \theta}{\partial z} - \frac{\partial u}{\partial z} \frac{\partial \theta}{\partial r} - \frac{\partial w}{\partial z} \frac{\partial \theta}{\partial z}. \quad (6)$$

The first two terms on the right-hand side of Eq. 6 represent advection of static stability by the radial and vertical wind, respectively. These terms act to rearrange the static stability field, but

²The validity of this approximation will be substantiated later in this section.

³These terms include the tendencies due to implicit diffusion in the fifth-order finite differencing scheme, which are separated from the advection

cannot strengthen or weaken static stability maxima or minima. The third and fourth terms on the right-hand side of Eq. 6 represent, respectively, the tilting of isentropes in the presence of vertical wind shear, and the stretching or squashing of isentropes by vertical gradients of vertical velocity. Since these terms involve velocity gradients, they can act to strengthen or weaken static stability maxima or minima through differential advection. Unless otherwise stated, any reference to "advection" in this paper indicates the sum of all of the terms in Eq. 6.

Returning to Eq. 5, HTURB and VTURB are the θ tendencies from the horizontal and vertical turbulence parameterizations, MP is the tendency from the microphysics scheme, RAD is the tendency from the radiation scheme, and DISS is the tendency due to turbulent dissipation. This equation neglects Rayleigh damping, since the entire analysis domain lies outside of the regions where damping is applied. Each term in Eq. 5 is substituted for $\partial\theta/\partial t$ in Eq. 4, yielding the contribution of each budget term to the static stability tendency. These terms are summed, yielding an instantaneous "budget change" in N^2 every minute. The budget changes are then averaged over 24-hour periods and compared to the total model change in N^2 over that same time period, i.e.:

$$\Delta N_{budget}^2 = \frac{1}{\delta t} \sum_{t=t_0}^{t_0+\delta t} \frac{\partial N^2}{\partial t} \bigg|_t \quad (7)$$

$$\Delta N_{model}^2 = N_{t_0+\delta t}^2 - N_{t_0}^2 \quad (8)$$

$$Residual = \Delta N_{model}^2 - \Delta N_{budget}^2 \quad (9)$$

where t_0 is an initial time and δt is 24 hours.

Eqs. 7-9 are plotted for three consecutive 24-hour periods in Fig. 2. For this and all subsequent radial-vertical cross sections, a 1-2-1 smoother is applied once in the radial direction to eliminate $2\Delta r$ noise that appears in some of the raw model output and calculated fields. The left column of Fig. 2 depicts the model changes computed using Eq. 8, together with Eq. 1 in saturated environments and Eq. 3 in subsaturated environments. The center column depicts the budget changes

155 computed using Eq. 7 together with Eq. 3 throughout the entire domain. Thus, the left column
 156 includes the effect of moisture in the N^2 computations, whereas the center column neglects mois-
 157 ture. The right column depicts the residuals, computed using Eq. 9 (i.e. the left column minus
 158 the center column.) In every 24-hour period, the budget changes are nearly identical to the model
 159 changes, which is reflected in the near-zero residuals in the right column. This indicates that the
 160 budget accurately represents the model variability, which implies that the neglect of moisture in
 161 the budget computation introduces negligible error within the analysis domain⁴.

162 In the tropopause layer, some of the budget terms are small enough to be ignored. To determine
 163 which of the budget terms are most important, a time series of the contribution of each of the
 164 budget terms in Eq. 5 to the tropopause-layer static stability tendency is plotted in Fig. 3. For this
 165 figure, each of the budget terms is computed using the method described in Section 3, except with
 166 1-hour averaging intervals instead of 24-hour intervals. The absolute values of these tendencies
 167 are then averaged over the radius-height domain of the plots shown in Fig. 2 and plotted as a time
 168 series⁵. Advection (Fig. 3, red line) plays an important role in the mean tropopause-layer static
 169 stability tendency at all times, and vertical turbulence (Fig. 3, blue line) and radiation (Fig. 3, dark
 170 green line) also contribute significantly. The remaining three processes - horizontal turbulence,
 171 microphysics, and dissipative heating - are negligible everywhere outside of the eyewall, and do
 172 not play important roles in the mesoscale tropopause variability.

173 The preceding analysis indicates that, at all times, three budget terms dominate the tropopause-
 174 layer static stability tendency: advection, vertical turbulence, and radiation. Variations in the

⁴This is not the case in the lower- and mid-troposphere, where the residual actually exceeds the budget tendencies in many places, likely due to the neglect of moisture; thus we limit this analysis to the upper troposphere and lower stratosphere.

⁵It will be seen in subsequent figures that each of the terms contributes both positively and negatively to the N^2 tendency within the analysis domain. Thus, taking an average over the domain tends to wash out the positive and negative contributions. To circumvent this problem, the absolute value of each of the terms is averaged.

175 magnitude and spatial structure of these terms drive the static stability changes depicted in Fig. 2;
176 subsequent sections will focus on these variations and what causes them.

177 **4. Results**

178 *a. Static stability evolution*

179 The average N^2 over the first day of the simulation (Fig. 4a) indicates the presence of a weak
180 N^2 maximum just above the cold-point tropopause. Over the subsequent 24 hours, during the
181 RI period, the N^2 within and above this layer decreased within the 25-km radius (Fig. 4b). This
182 decreasing N^2 corresponded to an increase in the tropopause height within the developing eye,
183 maximized at the storm center. Outside of the eye, meanwhile, the tropopause height decreased
184 over the eyewall region (25-60-km radius) and increased only slightly outside of the 60-km ra-
185 dius. In this outer region, the N^2 maximum just above the tropopause strengthened during RI.
186 These trends continued as the storm's intensity leveled off in the 48-72-hour period (Fig. 4c). The
187 tropopause height increased to nearly 21 km at the storm center and sloped sharply downward to
188 16.3 km on the inner edge of the eyewall, near the 30 km radius. Static stability outside of the eye,
189 meanwhile, continued to increase just above the cold-point tropopause. This N^2 evolution closely
190 follows that observed in Hurricane Patricia (2015; Duran and Molinari 2018, see their Fig. 4). The
191 mechanisms that led to these N^2 changes will be investigated in the subsequent sections.

192 *b. Static stability budget analysis*

193 *(i) 0-24 hours*

194 The initial spin-up period was characterized by a steady increase of the maximum wind speed
195 from 11 m s⁻¹ to 22 m s⁻¹ (Fig. 1a, blue line), an intensification rate that closely matched that of
196 TC Patricia (Fig. 1a, red stars). The weakening of the lower-stratospheric static stability maximum

197 during this period is reflected in the total N^2 budget change over this time (Fig. 5a). The layer just
 198 above the cold-point tropopause was characterized by decreasing N^2 (purple shading), maximizing
 199 at the storm center. At and immediately below the tropopause, meanwhile, N^2 increased during
 200 this time period (green shading). Although these tendencies extended out to the 200-km radius,
 201 they were particularly pronounced at innermost radii. A comparison of the contributions of advec-
 202 tion (Fig. 5b), vertical turbulence (Fig. 5c), and radiation (Fig. 5d) reveals that advection was the
 203 primary driver of the N^2 tendency during this period, acting to stabilize near and just below the
 204 tropopause and destabilize above. Although vertical turbulence acted in opposition to advection
 205 (i.e. it acted to stabilize regions that advection acted to destabilize), the magnitude of the advec-
 206 tive tendencies was larger, particularly at the innermost radii. The sum of advection and vertical
 207 turbulence (Fig. 5e) almost exactly replicated the static stability tendencies above the tropopause.
 208 Radiative tendencies, meanwhile, (Fig. 5d) acted to destabilize the layer below about 16 km and
 209 stabilize the layer between 16 and 17 km. The sum of advection, vertical turbulence, and radiation
 210 (Fig. 5f) reproduced the total change in N^2 almost exactly.

211 (ii) 24-48 hours

212 During the RI period, the maximum wind speed increased from 22 m s⁻¹ to 80 m s⁻¹ (Fig. 1a).
 213 Over this time, N^2 within the eye generally decreased above 16 km and increased below (Fig. 6a),
 214 with the destabilization above 16 km maximizing near the level of the mean cold-point tropopause.
 215 These tendencies at the innermost radii were driven almost entirely by advection (Fig. 6b). Vertical
 216 turbulence (Fig. 6c) and radiation (Fig. 6d) contributed negligibly to the static stability tendencies
 217 in this region.

218 Outside of the eye, the N^2 evolution exhibited alternating layers of positive and negative tenden-
 219 cies. Near and above 18 km existed an upward-sloping region of decreasing N^2 that extended out

220 to the 180-km radius. In this region, neither vertical turbulence nor radiation exhibited negative N^2
 221 tendencies; advection was the only forcing for this destabilization. Immediately below this layer,
 222 just above the cold-point tropopause, was a region of increasing N^2 that sloped upward from 17
 223 km near the 30-km radius to just below 18 km outside of the 100-km radius. Advection and verti-
 224 cal turbulence both contributed to this positive N^2 tendency, with advection playing an important
 225 role below about 17.5 km and and turbulence playing an important role above. The sum of advec-
 226 tion and turbulence (Fig. 6e) reveals two separate regions of increasing N^2 in the 17-18-km layer
 227 rather than one contiguous region. The addition of radiation to these two terms, however, (Fig. 6f)
 228 provides the link between these two regions, indicating that radiation also plays a role in strength-
 229 ening the stable layer just above the tropopause. In the 16-17-km layer, just below the cold-point
 230 tropopause, a horizontally-extensive layer of destabilization also was forced by a combination of
 231 advection, vertical turbulence, and radiation. The sum of advection and vertical turbulence ac-
 232 counts for only a portion of the decreasing N^2 in this layer, and actually indicates forcing for
 233 stabilization near the 50-km radius and outside of the 130-km radius. Radiative tendencies over-
 234 come this forcing for stabilization in both of these regions to produce the radially-extensive region
 235 of destabilization observed just below the tropopause.

236 The sum of advection, vertical turbulence, and radiation (Fig. 6f) once again closely follows
 237 the observed N^2 variability, except in the eyewall region, where the neglect of latent heating and
 238 horizontal turbulence introduces some differences.

239 (iii) 48-72 hours

240 After the storm's maximum wind speed leveled off near 80 m s^{-1} (Fig. 1a), the magnitude of
 241 the static stability tendencies within the eye decreased to near zero (Fig. 7a). Outside of the eye,
 242 however, N^2 continued to decrease in the layer immediately surrounding the tropopause and in-

crease just above. The sum of advection and vertical turbulence (Fig. 7e) indicates that these two processes account for most of the destabilization near the tropopause and some of the stabilization near the 18-km altitude. Below the tropopause, however, these two terms provided strong forcing for stabilization that was not observed in the budget change (Fig. 7a). Radiation (Fig. 7d), which generally forced stabilization above 17 km and destabilization below, balanced out this forcing for stabilization in the upper troposphere. In the eyewall region (30-80-km radius), advection and vertical turbulence combined to force destabilization in the 17-18-km layer (Fig. 7e), which was not observed in the budget change (Fig. 7a). Radiation provided strong forcing for stabilization, which outweighed this effect and produced net stabilization in a portion of this region. Outside of the 80-km radius, both advection (Fig. 7b) and vertical turbulence (Fig. 7c) provided forcing for stabilization near and just above the 18-km level. The sum of the two terms (Fig. 7e) indicates increasing N^2 near the 18-km level everywhere outside of the 80-km radius, but this stabilization is slightly weaker in the 90-120-km radial band than the observed value. The addition of radiation (Fig. 7f) provided the extra forcing for stabilization required to account for the observed increase in N^2 . Outside of the 120-km radius, the region of radiative forcing for stabilization sloped downward, and the increase in N^2 observed near 18 km can be explained entirely by a combination of advection and vertical turbulence.

5. Discussion

a. The role of advection

Advection played an important role in the tropopause-layer N^2 evolution at all stages of intensification, but for brevity, this section will focus only on the RI (24-48-hour) period. To investigate the advective processes more closely, the individual contributions of horizontal and vertical advection

265 during the RI period are shown in Fig. 8, along with the corresponding time-mean radial and verti-
266 cal velocities and θ . The N^2 tendencies due to the two advective components (Fig. 8a,b) exhibited
267 strong cancellation, consistent with flow that was nearly isentropic. There existed, however, a
268 large region near the tropopause in which the total advective tendency was nonzero (Fig. 6b).
269 These nonzero tendencies were related to the development of the TC's secondary circulation as
270 the storm intensified.

271 During the RI period, strong radial and vertical circulations developed near the tropopause
272 (Fig. 8c,d), which forced high-magnitude N^2 tendencies due to advection (Fig. 8a,b). A layer
273 of strong outflow formed at and below the tropopause during this period, with the outflow maxi-
274 mum (dashed cyan line) curving from the 14-km level at the 50-km radius to just below the 16-km
275 level outside of the 80-km radius (Fig. 8c). Notably, the N^2 tendency due to horizontal advection
276 (Fig. 8a) tended to switch signs at this line, with stabilization below the outflow maximum and
277 destabilization above. This is consistent with the outflow layer carrying air with increasingly large
278 θ from the eyewall to large radii as the storm intensified. This increase in θ maximized near the
279 outflow maximum, which acted to decrease $\partial\theta/\partial z$ above the outflow maximum and increase it be-
280 low. This mechanism is the same as that discussed in Trier and Sharman (2009), in which vertical
281 wind shear in the outflow layer of a mesoscale convective system modified the upper-tropospheric
282 static stability through differential advection of isentropes.

283 Meanwhile in the lower stratosphere, a thin layer of 2-4 m s⁻¹ inflow developed a few hundred
284 meters above the tropopause, similar to that which was observed in Hurricane Patricia (2015;
285 Duran and Molinari 2018) and in previous modeling studies (e.g. Ohno and Satoh 2015; Kieu et al.
286 2016). Since the isentropes in this layer sloped slightly upward with radius (i.e. $\partial\theta/\partial r < 0$), this
287 inflow acted to import lower θ air from outer radii to inner radii. Since the negative θ tendencies

288 maximized at the level of maximum inflow, the layer below the inflow maximum destabilized and
289 the layer above stabilized (Fig. 8a).

290 Curiously, horizontal advection contributed to the N^2 tendency everywhere within the eye,
291 even though the mean radial velocity there was near zero. Close examination of the model out-
292 put revealed that these tendencies were forced by advective processes associated with inward-
293 propagating waves. Although the radial velocity perturbations induced by these waves averaged
294 out to zero, the advective tendencies forced by the radial velocity perturbations did not. Addition-
295 ally, when these waves reached $r=0$, a dipole of vertical velocity resulted, with ascent above and
296 descent below. For reasons that remain unclear, the regions of ascent were more persistent than the
297 regions of descent, which resulted in the mean ascent observed near $r=0$ above 17 km in Fig. 8d.

298 Vertical advection also played an important role in the tropopause-layer static stability evolution.
299 Within the eye, subsidence dominated below 17 km, while mean ascent existed near the storm
300 center above 17 km. Although the magnitude of the subsidence was larger at lower altitudes,
301 $\partial\theta/\partial z$ was smaller there. Because $\partial\theta/\partial z$ was smaller, the subsidence at lower levels could not
302 accomplish as much warming as the subsidence at higher levels in the eye, consistent with the
303 results of Stern and Zhang (2013). As a result, vertical advection within the eye stabilized the
304 layer below 16 km during RI.

305 Outside of the 27-km radius, ascent dominated the troposphere, while a 1-1.5-km-deep layer
306 of descent existed immediately above the tropopause. These regions of ascent and descent con-
307 verged just above the tropopause; this convergence acted to compact the isentropes in this layer
308 and increase the static stability. Above the lower-stratospheric subsidence maximum, meanwhile,
309 vertical advection decreased N^2 . Below the tropopause, differential vertical advection increased
310 N^2 within the eyewall region and also at larger radii above the vertical velocity maximum at larger

311 radii. Outside of the eyewall and below the vertical velocity maximum, meanwhile, differential
312 vertical advection acted to decrease N^2 .

313 Comparing the N^2 tendencies forced by horizontal (Fig. 8a) and vertical (Fig. 8b) advection
314 to the total advective tendency seen in Fig. 6b reveals that horizontal advective tendencies domi-
315 nated the troposphere, while vertical advective tendencies dominated the layer near and above the
316 tropopause. Thus, tilting of isentropes in the vicinity of the upper-tropospheric outflow maximum
317 appears to be the most important advective process governing the N^2 tendency in the troposphere,
318 whereas convergence of vertical velocity appears to be the most important advective process near
319 the tropopause.

320 *b. The role of radiation*

321 During the initial spin-up period (0-24 hours; Fig. 9a), convection was not deep enough to
322 deposit large quantities of ice near the tropopause and create a persistent cirrus canopy. Due to the
323 lack of ice particles, the radiative heating tendencies during this period (Fig. 9b) were relatively
324 small and confined to the region above a few particularly strong, although transient, convective
325 towers. During RI (24-48 hours), the eyewall updraft strengthened and a radially-extensive cirrus
326 canopy developed near the tropopause (Fig. 9c). The enhanced vertical gradient of ice mixing ratio
327 at the top of the cirrus canopy induced strong diurnal-mean radiative cooling near the tropopause
328 (Fig. 9d). This cooling exceeded 0.6 K h^{-1} (14.4 K day^{-1}) in some places and sloped downward
329 from the lower stratosphere into the upper troposphere, following the top of the cirrus canopy. A
330 small radiative warming maximum also appeared outside of the 140-km radius below this region
331 of cooling. These results broadly agree with those of Bu et al. (2014; see their Fig. 11a), whose
332 CM1 simulations produced a 0.3 K h^{-1} diurnally-averaged radiative cooling at the top of the cirrus
333 canopy and radiative warming within the cloud that maximized near the 200-km radius. This broad

334 region of radiative cooling acted to destabilize the layer below the cooling maximum and stabilize
335 the layer above, which can be seen in Fig. 6d. The small area of net radiative heating outside of
336 the 140-km radius enhanced the destabilization above 16 km in this region and produced a thin
337 layer of stabilization in the 15-16-km layer.

338 After the TC's RI period completed (48-72 hours), strong radiative cooling remained near the
339 tropopause at inner radii (Fig. 9f), sloping downward with the top of the cirrus canopy to below the
340 tropopause at outer radii. Cooling rates exceeded 1 K h^{-1} (24 K day^{-1}) just above the tropopause
341 between the 30- and 70-km radii. This value is more than three times the maximum cooling rate of
342 0.3 K h^{-1} observed by Bu et al. (2014), a difference that is a consequence of their larger vertical grid
343 spacing compared to that used here, along with a contribution from differing radiation schemes.
344 To compare our results to theirs, we ran a simulation identical to that described in Section 2, except
345 using the NASA-Goddard radiation scheme and 625-m vertical grid spacing, to match those of Bu
346 et al. (2014). This simulation produced a maximum 24-hour-average radiative cooling rate of 0.3
347 K h^{-1} , which agrees with that shown in Bu et al. (2014). Another simulation using 625-m vertical
348 grid spacing and RRTMG radiation produced 24-hour-average cooling rates of up to 0.6 K h^{-1} .
349 This suggests that vertical grid spacing smaller than 625 m is necessary to resolve properly the
350 radiative cooling at the top of the cirrus canopy, and that the results can be quite sensitive to the
351 radiation scheme used.

352 Meanwhile below the tropopause, time-mean radiative warming spread from 30- to 160-km
353 radius within the cirrus canopy. The existence of radiative cooling overlying radiative warming in
354 this region led to radiatively-forced destabilization at and below the tropopause, as was observed
355 in Fig. 7d. Beneath the warming layer existed a region of forcing for stabilization, while a much
356 stronger region of forcing for stabilization existed in the lower stratosphere, above the cooling
357 maximum.

358 The results herein suggest that, after the cirrus canopy developed, radiative heating tendencies
359 considerably destabilized the upper troposphere and stabilized the lower stratosphere.

360 *c. The role of turbulent mixing*

361 Fig. 10 depicts the effect of turbulent mixing on the vertical θ profile of an initially stably-
362 stratified layer. At the initial time in this schematic, θ is assumed to increase with height at a
363 constant rate (Fig. 10, left panel). The imposition of turbulence (blue hatching) adjusts the θ
364 profile within the mixed layer toward a constant value equal to the mean value of that layer in
365 the initial state (Fig. 10, right panel). Just above and just below the mixed layer, however, the θ
366 profile remains undisturbed. Consequently, although turbulent mixing acts to decrease $\partial\theta/\partial z$ in
367 the layer in which it is occurring, it actually increases $\partial\theta/\partial z$ just below and just above the layer.
368 Vertical gradients of turbulent mixing like those depicted here are quite important, particularly on
369 the flanks of the upper-tropospheric outflow jet.

370 Two distinct maxima of vertical eddy diffusivity developed in the tropopause layer as the storm
371 intensified (Fig. 11). Comparison of these turbulent regions to the N^2 tendencies in Figs. 6c and
372 7c reveals that the layers in which vertical eddy diffusivity maximized corresponded to layers of
373 destabilization due to vertical turbulence. Just outside of these layers, however, vertical turbulence
374 acted to increase N^2 . The large vertical gradient of vertical eddy diffusivity near the tropopause
375 played an important role in developing the lower-stratospheric stable layer during RI. These results
376 support the hypothesized role of turbulence in setting the outflow-layer θ stratification in Emanuel
377 and Rotunno (2011).

6. Conclusions

The simulated N^2 evolution shown herein closely matched that observed during the RI of Hurricane Patricia (2015). Three N^2 budget terms dominated in the upper troposphere and lower stratosphere: advection, radiation, and vertical turbulence. Advection dominated within the eye, where it provided forcing for destabilization. Radiation and vertical turbulence played particularly important roles in developing the strong N^2 maximum just above the cold-point tropopause during RI.

To put the N^2 variability observed near the tropopause into context, Fig. 12 depicts the model change in N^2 over the RI period (hours 24-48) from 0 to 21 km altitude, along with the vertical eddy diffusivity and the radiative heating rate. The largest changes in N^2 occurred in a relatively shallow layer immediately surrounding the tropopause (Fig. 12a). This shallow layer also contained the largest diurnally-averaged radiative heating tendencies found anywhere in the domain (Fig. 12c). Values of vertical eddy diffusivity larger than any found outside of the boundary layer also resided in the upper troposphere (Fig. 12b). The results herein suggest that this turbulence not only develops as a response to the presence of small static stability and large vertical wind shear, as discussed by Molinari et al. (2014) and Duran and Molinari (2016), but also can actively increase the static stability in highly localized regions just above and below the mixed layers.

Since two of the most important processes contributing to the N^2 variability are parameterized, and one (radiation) closely depends on yet another parameterized process (microphysics), the tropopause-layer N^2 variability could be quite sensitive to the assumptions inherent to the parameterizations used. A better understanding of the microphysical characteristics of the TC cirrus canopy, its interaction with radiation, and outflow-layer turbulence is critical to understanding the tropopause-layer N^2 evolution.

401 In this paper, all of the variables were averaged over a full diurnal cycle to eliminate the effects
402 of diurnal variability and isolate the overall storm evolution. Diurnal variations in static stability
403 near the tropopause are potentially of interest with respect to the tropical cyclone diurnal cycle,
404 and will be the subject of future work.

405 *Acknowledgments.* We are indebted to George Bryan for his continued development and support
406 of Cloud Model 1. We also thank Jeffrey Kepert, Robert Fovell, and Erika Navarro for helpful
407 conversations related to this work. This research was supported by NSF grant AGS-1636799 and
408 Office of Naval Research Grant N000141712110 as a part of the TCI Departmental Research
409 Initiative.

410 **References**

- 411 Bryan, G. H., cited 2018: The governing equations for CM1. [Available online at http://www2.mmm.ucar.edu/people/bryan/cm1/cm1_equations.pdf].
- 412
- 413 Bryan, G. H., and R. Rotunno, 2009: The maximum intensity of tropical cyclones in axisymmetric
414 numerical model simulations. *Mon. Wea. Rev.*, **137**, 1770–1789.
- 415 Bu, Y. P., R. G. Fovell, and K. L. Corbosiero, 2014: Influence of cloud-radiative forcing on tropical
416 cyclone structure. *J. Atmos. Sci.*, **71**, 1644–1622.
- 417 Doyle, J. D., and Coauthors, 2017: A view of tropical cyclones from above: The Tropical Cyclone
418 Intensity (TCI) Experiment. *Bull. Amer. Meteor. Soc.*, **98**, 2113–2134.
- 419 Duran, P., and J. Molinari, 2016: Upper-tropospheric low Richardson number in tropical cyclones:
420 Sensitivity to cyclone intensity and the diurnal cycle. *J. Atmos. Sci.*, **73**, 545–554.
- 421 Duran, P., and J. Molinari, 2018: Dramatic inner-core tropopause variability during the rapid
422 intensification of Hurricane Patricia (2015). *Mon. Wea. Rev.*, **146**, 119–134.

423 Emanuel, K., 2012: Self-stratification of tropical cyclone outflow. Part II: Implications for storm
 424 intensification. *J. Atmos. Sci.*, **69**, 988–996.

425 Emanuel, K., and R. Rotunno, 2011: Self-stratification of tropical cyclone outflow. Part I: Impli-
 426 cations for storm structure. *J. Atmos. Sci.*, **68**, 2236–2249.

427 Iacono, M. J., J. S. Delamere, E. J. Mlawer, M. W. Shephard, S. A. Clough, and W. D. Collins,
 428 2008: Radiative forcing by long-lived greenhouse gases: Calculations with the AER radiative
 429 transfer models. *J. Geophys. Res.*, **113** (D13103).

430 Kepert, J. D., J. Schwendike, and H. Ramsay, 2016: Why is the tropical cyclone boundary layer
 431 not ”well mixed”? *J. Atmos. Sci.*, **73**, 957–973.

432 Kieu, C., V. Tallapragada, D.-L. Zhang, and Z. Moon, 2016: On the development of double warm-
 433 core structures in intense tropical cyclones. *J. Atmos. Sci.*, **73**, 4487–4506.

434 Kimberlain, T. B., E. S. Blake, and J. P. Cangialosi, 2016: Tropical cyclone report: Hurricane
 435 Patricia. National Hurricane Center. [Available online at www.nhc.noaa.gov].

436 Komaromi, W. A., and J. D. Doyle, 2017: Tropical cyclone outflow and warm core structure as
 437 revealed by HS3 dropsonde data. *Mon. Wea. Rev.*, **145**, 1339–1359.

438 Markowski, P. M., and G. H. Bryan, 2016: LES of laminar flow in the PBL: A potential problem
 439 for convective storm simulations. *Mon. Wea. Rev.*, **144**, 1841–1850.

440 Molinari, J., P. Duran, and D. Vollaro, 2014: Low Richardson number in the tropical cyclone
 441 outflow layer. *J. Atmos. Sci.*, **71**, 3164–3179.

442 Ohno, T., and M. Satoh, 2015: On the warm core of a tropical cyclone formed near the tropopause.
 443 *J. Atmos. Sci.*, **72**, 551–571.

444 Rogers, R. F., S. Aberson, M. M. Bell, D. J. Cecil, J. D. Doyle, J. Morgerman, L. K. Shay, and
 445 C. Velden, 2017: Re-writing the tropical record books: The extraordinary intensification of
 446 Hurricane Patricia (2015). *Bull. Amer. Meteor. Soc.*, **98**, 2091–2112.

447 Rotunno, R., and K. A. Emanuel, 1987: An air-sea interaction theory for tropical cyclones. Part II:
 448 Evolutionary study using a nonhydrostatic axisymmetric numerical model. *J. Atmos. Sci.*, **44**,
 449 542–561.

450 Stern, D. P., and F. Zhang, 2013: How does the eye warm? Part I: A potential temperature budget
 451 analysis of an idealized tropical cyclone. *J. Atmos. Sci.*, **70**, 73–89.

452 Thompson, G., R. M. Rasmussen, and K. Manning, 2004: Explicit forecasts of winter precipitation
 453 using an improved bulk microphysics scheme. Part I: Description and sensitivity analysis. *Mon.*
 454 *Wea. Rev.*, **132**, 519–542.

455 Trier, S. B., and R. D. Sharman, 2009: Convection-permitting simulations of the environment sup-
 456 porting widespread turbulence within the upper-level outflow of a mesoscale convective system.
 457 *Mon. Wea. Rev.*, **137**, 1972–1990.

LIST OF FIGURES

- Fig. 1.** The maximum 10-m wind speed (top panel; m s^{-1}) and minimum sea-level pressure (bottom panel; hPa) in the simulated storm (blue lines; plotted every minute) and from Hurricane Patricia's best track (red stars; plotted every six hours beginning at the time Patricia attained tropical storm intensity). The rapid weakening during the later stage of Patricia's lifetime was induced by landfall. 25
- Fig. 2.** Left panels: Twenty-four-hour changes in squared Brunt-Väisälä frequency (N^2 ; 10^{-4} s^{-2}) computed using Eq. 8 over (top row) 0-24 hours, (middle row) 24-48 hours, (bottom row) 48-72 hours. Middle Panels: The N^2 change over the same time periods computed using Eqs. 4-7, Right Panels: The budget residual over the same time periods, computed by subtracting the budget change (middle column) from the model change (left column). Orange lines represent the cold-point tropopause height averaged over the same time periods. 26
- Fig. 3.** Time series of the contribution of each of the budget terms to the time tendency of the squared Brunt-Väisälä frequency (N^2 ; 10^{-4} s^{-2}). For each budget term, the absolute value of the N^2 tendency is averaged temporally over 1-hour periods (using output every minute), and spatially in a region extending from 0 to 200 km radius and 14 to 21 km altitude. 27
- Fig. 4.** Twenty-four-hour averages of squared Brunt-Väisälä frequency (N^2 ; 10^{-4} s^{-2}) over (a) 0-24 hours, (b) 24-48 hours, (c) 48-72 hours. Orange lines represent the cold-point tropopause height averaged over the same time periods. 28
- Fig. 5.** (a) Total change in N^2 over the 0-24-hour period ($10^{-4} \text{ s}^{-2} (24 \text{ h})^{-1}$) and the contributions to that change from (b) the sum of horizontal and vertical advection, (c) vertical turbulence, (d) longwave and shortwave radiation, (e) the sum of horizontal advection, vertical advection, and vertical turbulence, and (f) the sum of horizontal advection, vertical advection, vertical turbulence, and longwave and shortwave radiation. Green shading indicates regions of stabilization and purple shading indicates regions of destabilization. Orange lines represent the cold-point tropopause height averaged over the 0-24-hour period. 30
- Fig. 6.** As in Fig. 5, but for the 24-48-hour period. 31
- Fig. 7.** As in Fig. 5, but for the 48-72-hour period. 32
- Fig. 8.** The contributions to the change in N^2 over the 24-48-hour period ($10^{-4} \text{ s}^{-2} (24 \text{ h})^{-1}$) by (a) horizontal advection and (b) vertical advection. (c) The radial velocity (m s^{-1} ; filled contours), potential temperature (K; thick black contours), cold-point tropopause height (orange line), and level of maximum outflow (dashed cyan line) averaged over the 24-48-hour period. (d) The vertical velocity (cm s^{-1} ; filled contours), potential temperature (K; thick black contours), and cold-point tropopause height (orange line) averaged over the 24-48-hour period. 33
- Fig. 9.** Ice mixing ratio (g kg^{-1}) and cold-point tropopause height (orange lines) averaged over (a) 0-24 hours, (c) 24-48 hours, and (e) 48-72 hours. Radiative heating rate (K h^{-1}) and cold-point tropopause height (orange lines) averaged over (b) 0-24 hours, (d) 24-48 hours, and (f) 48-72 hours. 35
- Fig. 10.** Schematic diagram of the effect of turbulent mixing on the vertical profile of potential temperature (θ). At the initial time (left panel), potential temperature is assumed to increase with height at a constant rate (thick black line). The imposition of turbulence within a portion of the layer (blue hatching) adjusts the potential temperature profile toward the mean

501 initial value of that layer. After a period of mixing (right panel) the potential temperature in
 502 the mixed layer does not vary with height, but just above and just below the mixed layer, it
 503 rapidly increases with height. 36

504 **Fig. 11.** Vertical eddy diffusivity ($\text{m}^2 \text{s}^{-2}$; filled contours), cold-point tropopause height (cyan lines),
 505 and radial velocity (m s^{-1} ; thick black lines) averaged over (a) 0-24 hours, (b) 24-48 hours,
 506 and (c) 48-72 hours. 37

507 **Fig. 12.** (Top panel) Change in N^2 over the 24-48-hour period ($10^{-4} \text{s}^{-2} (24 \text{ h})^{-1}$) directly output by
 508 the model for the 0-21-km layer. (Middle panel) Vertical eddy diffusivity ($\text{m}^2 \text{s}^{-2}$) averaged
 509 over the same time period. (Bottom panel) Radiative heating rate (K h^{-1}) averaged over the
 510 same time period. 39

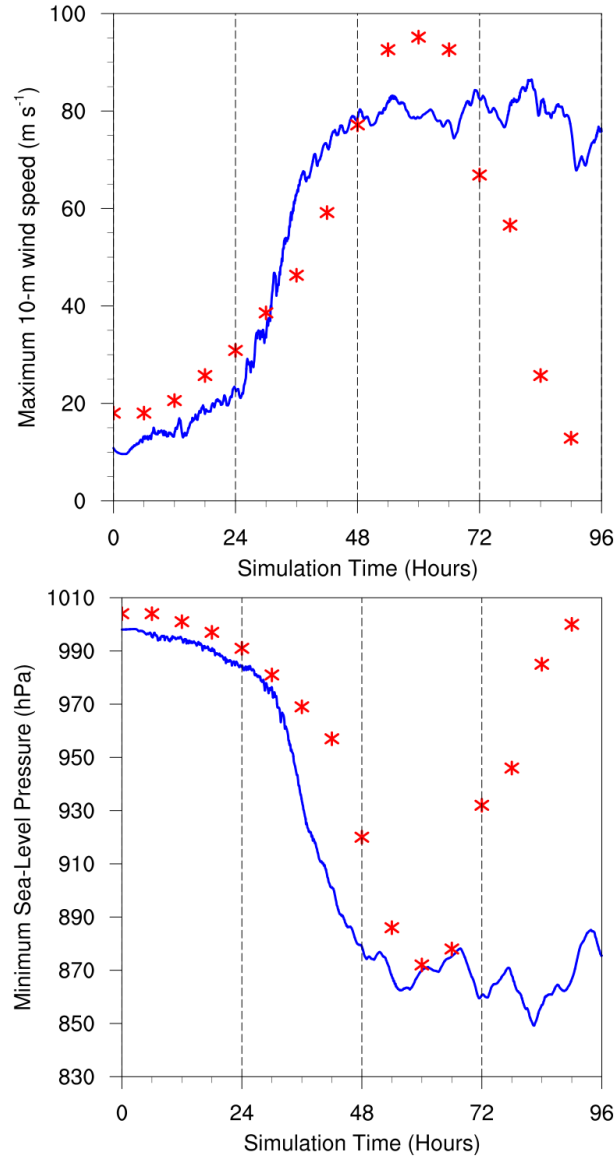


FIG. 1. The maximum 10-m wind speed (top panel; m s^{-1}) and minimum sea-level pressure (bottom panel; hPa) in the simulated storm (blue lines; plotted every minute) and from Hurricane Patricia's best track (red stars; plotted every six hours beginning at the time Patricia attained tropical storm intensity). The rapid weakening during the later stage of Patricia's lifetime was induced by landfall.

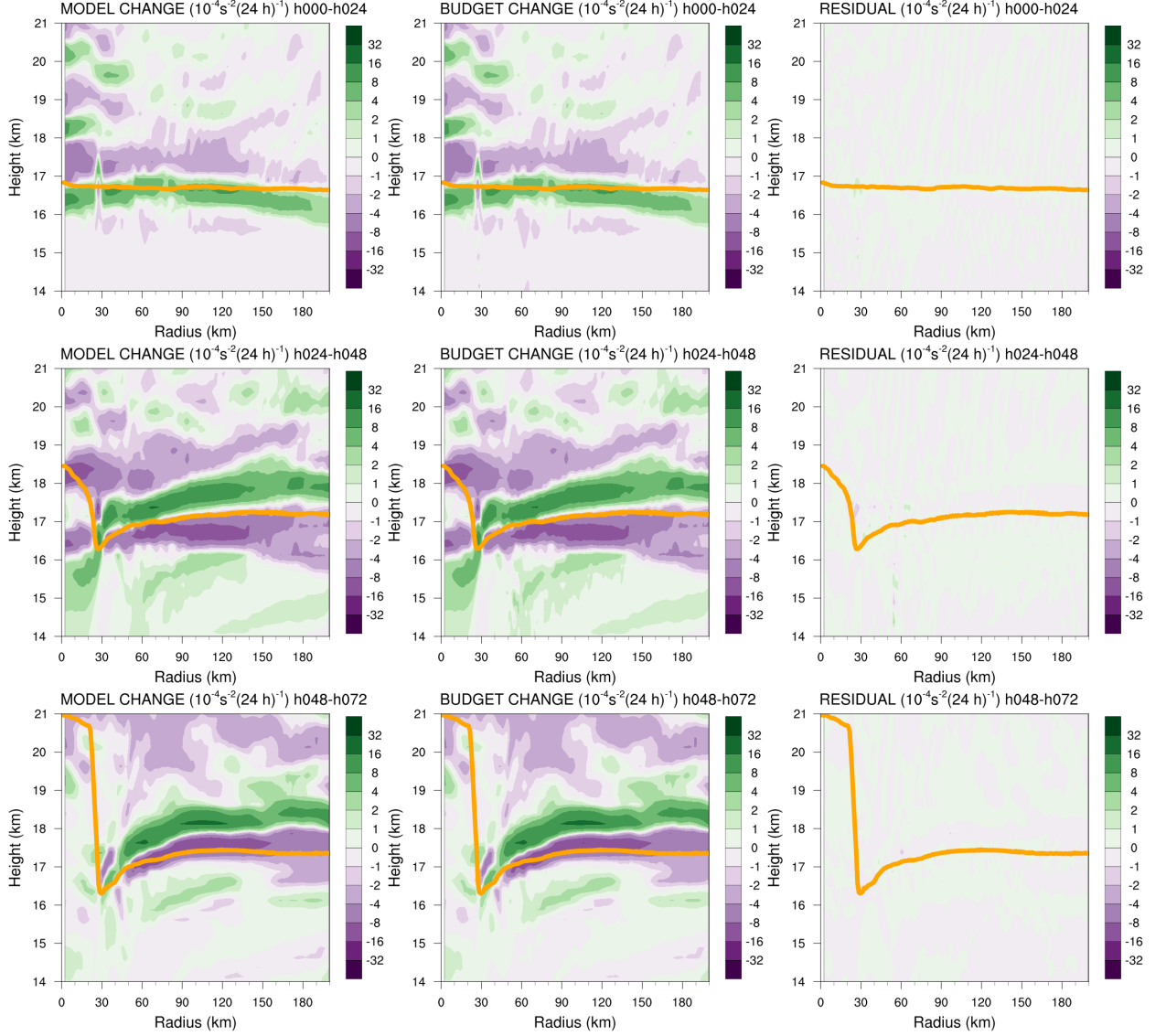


FIG. 2. Left panels: Twenty-four-hour changes in squared Brunt-Väisälä frequency (N^2 ; 10^{-4} s^{-2}) computed using Eq. 8 over (top row) 0-24 hours, (middle row) 24-48 hours, (bottom row) 48-72 hours. Middle Panels: The N^2 change over the same time periods computed using Eqs. 4-7, Right Panels: The budget residual over the same time periods, computed by subtracting the budget change (middle column) from the model change (left column). Orange lines represent the cold-point tropopause height averaged over the same time periods.

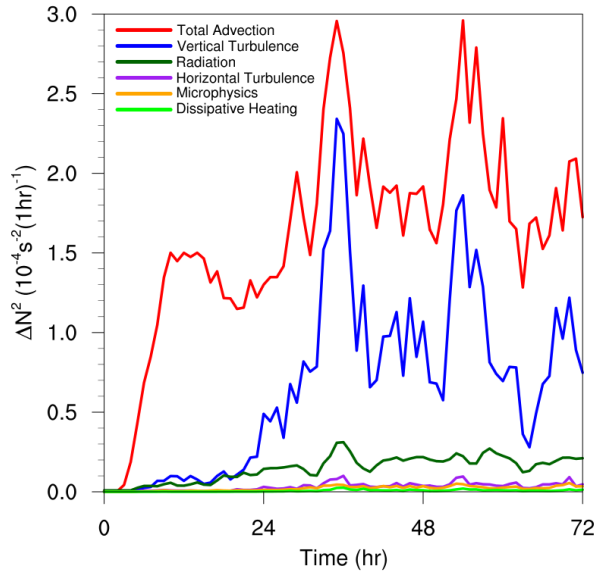


FIG. 3. Time series of the contribution of each of the budget terms to the time tendency of the squared Brunt-Väisälä frequency (N^2 ; 10^{-4} s^{-2}). For each budget term, the absolute value of the N^2 tendency is averaged temporally over 1-hour periods (using output every minute), and spatially in a region extending from 0 to 200 km radius and 14 to 21 km altitude.

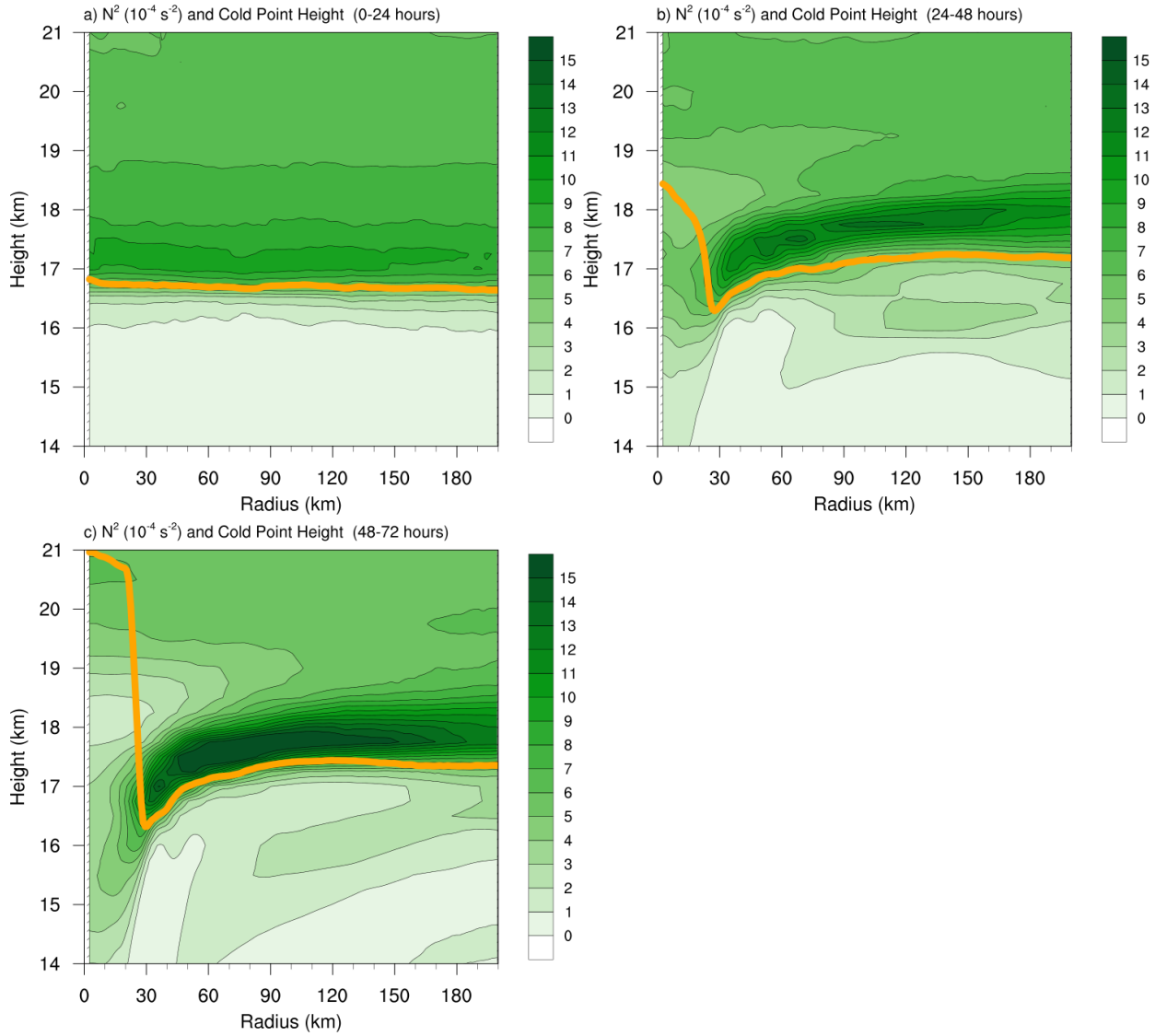
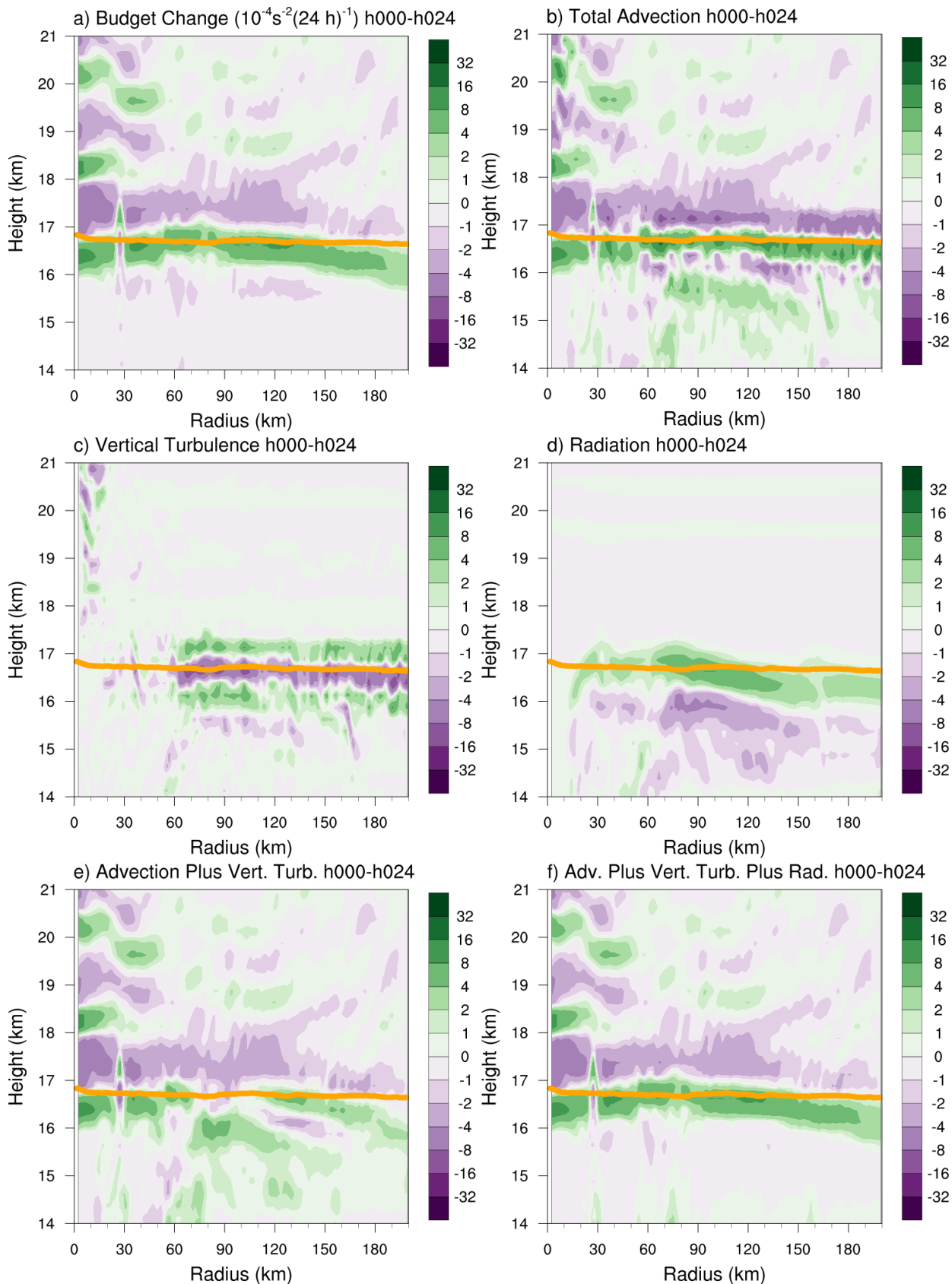


FIG. 4. Twenty-four-hour averages of squared Brunt-Väisälä frequency (N^2 ; 10^{-4} s^{-2}) over (a) 0-24 hours, (b) 24-48 hours, (c) 48-72 hours. Orange lines represent the cold-point tropopause height averaged over the same time periods.



527 FIG. 5. (a) Total change in N^2 over the 0-24-hour period ($10^{-4} \text{ s}^{-2} (24 \text{ h})^{-1}$) and the contributions to that change
 528 from (b) the sum of horizontal and vertical advection, (c) vertical turbulence, (d) longwave and shortwave
 529 radiation, (e) the sum of horizontal advection, vertical advection, and vertical turbulence, and (f) the sum of
 530 horizontal advection, vertical advection, vertical turbulence, and longwave and shortwave radiation. Green
 531 shading indicates regions of stabilization and purple shading indicates regions of destabilization. Orange lines
 532 represent the cold-point tropopause height averaged over the 0-24-hour period.

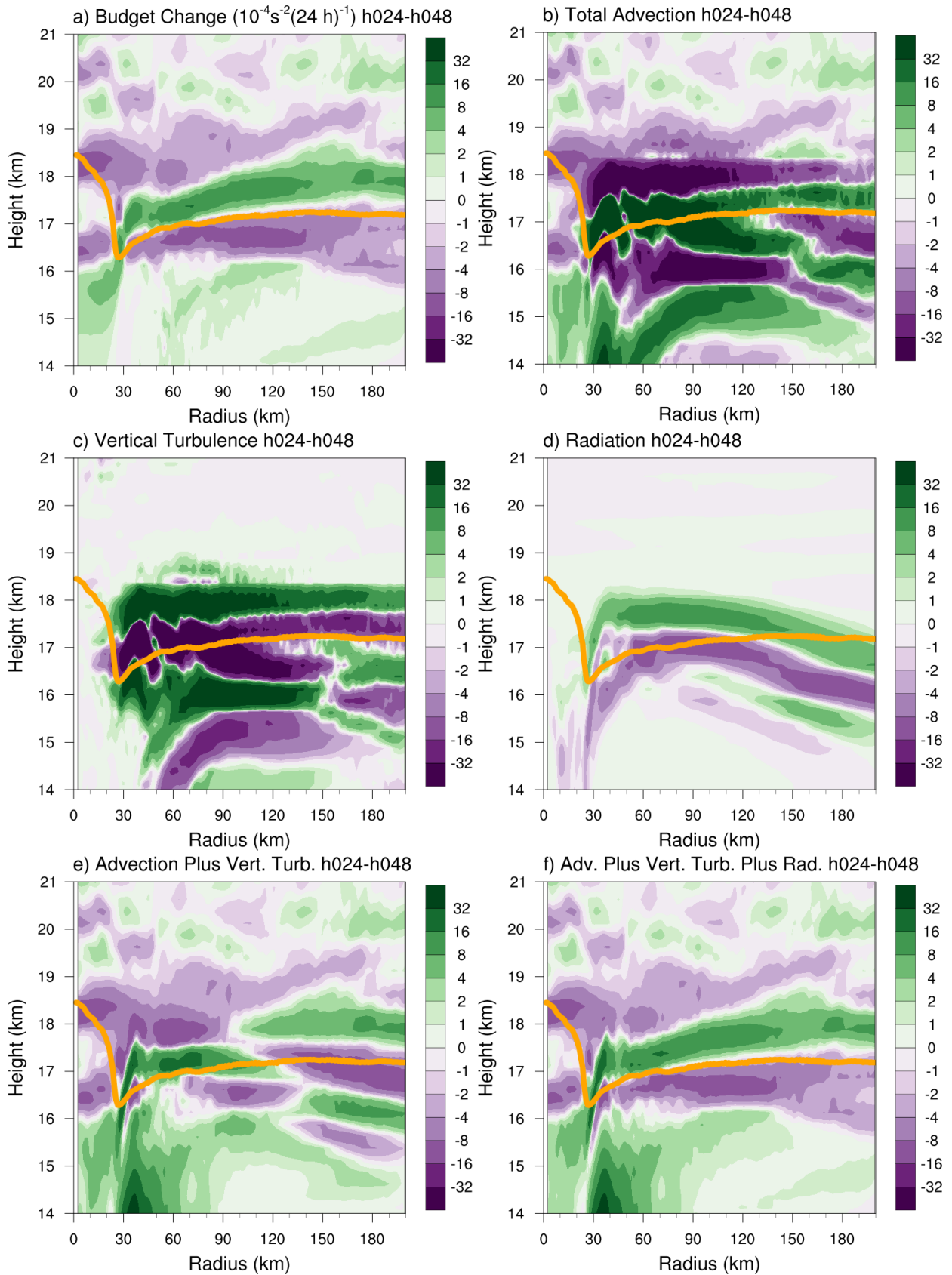


FIG. 6. As in Fig. 5, but for the 24-48-hour period.

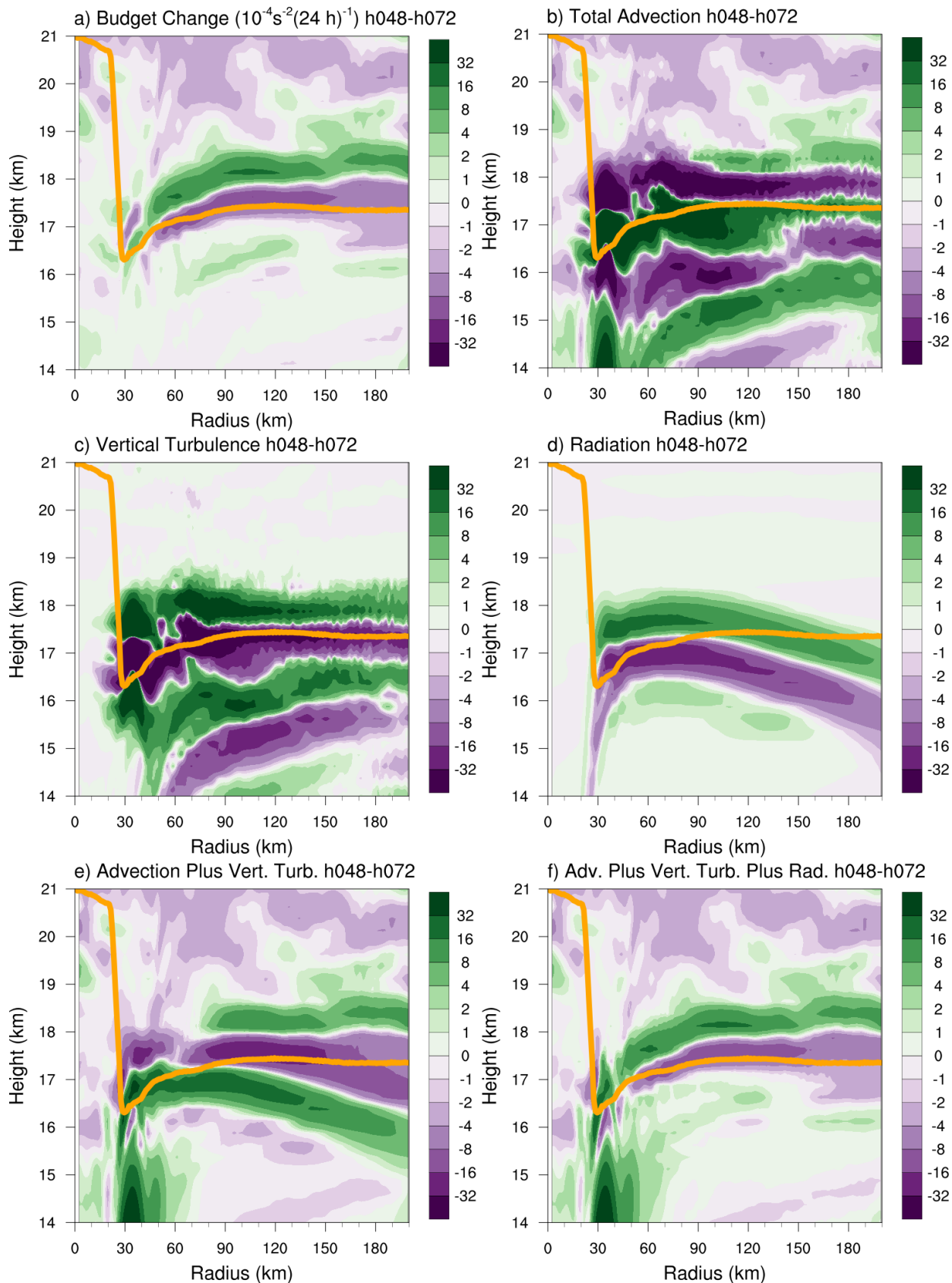


FIG. 7. As in Fig. 5, but for the 48-72-hour period.

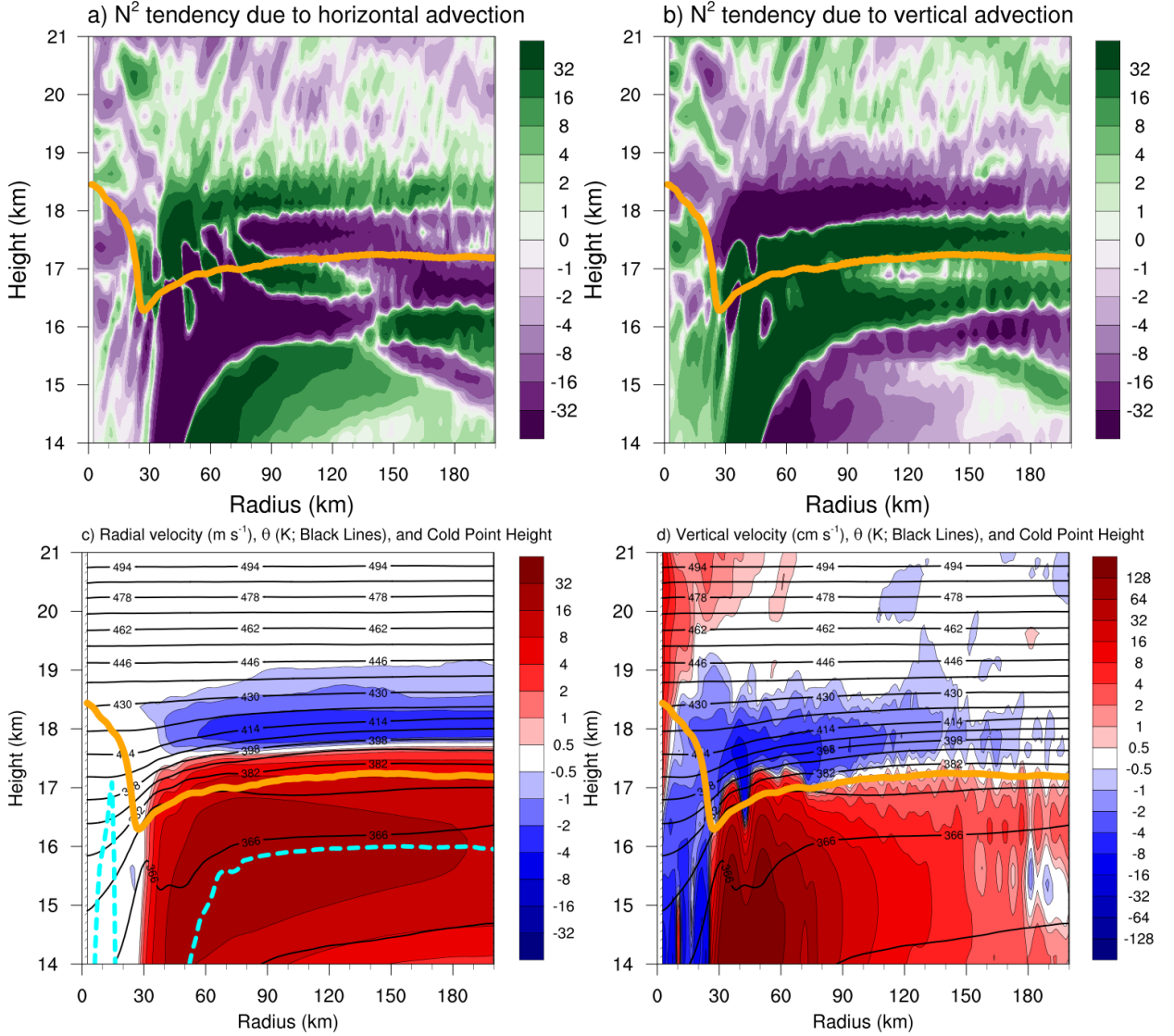
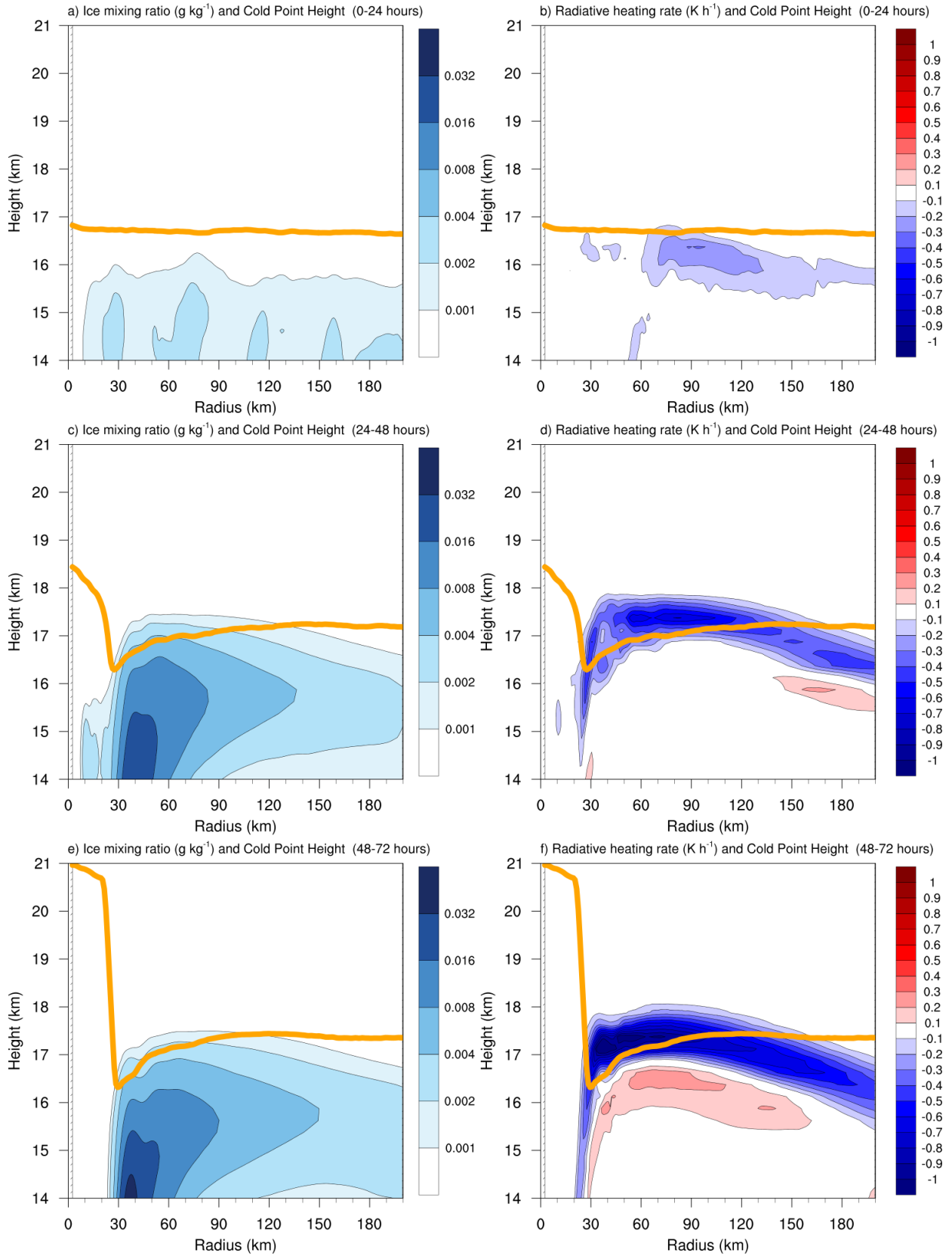


FIG. 8. The contributions to the change in N^2 over the 24-48-hour period ($10^{-4} \text{ s}^{-2} (24 \text{ h})^{-1}$) by (a) horizontal advection and (b) vertical advection. (c) The radial velocity (m s^{-1} ; filled contours), potential temperature (K; thick black contours), cold-point tropopause height (orange line), and level of maximum outflow (dashed cyan line) averaged over the 24-48-hour period. (d) The vertical velocity (cm s^{-1} ; filled contours), potential temperature (K; thick black contours), and cold-point tropopause height (orange line) averaged over the 24-48-hour period.



539 FIG. 9. Ice mixing ratio (g kg^{-1}) and cold-point tropopause height (orange lines) averaged over (a) 0-24 hours,
540 (c) 24-48 hours, and (e) 48-72 hours. Radiative heating rate (K h^{-1}) and cold-point tropopause height (orange
541 lines) averaged over (b) 0-24 hours, (d) 24-48 hours, and (f) 48-72 hours.

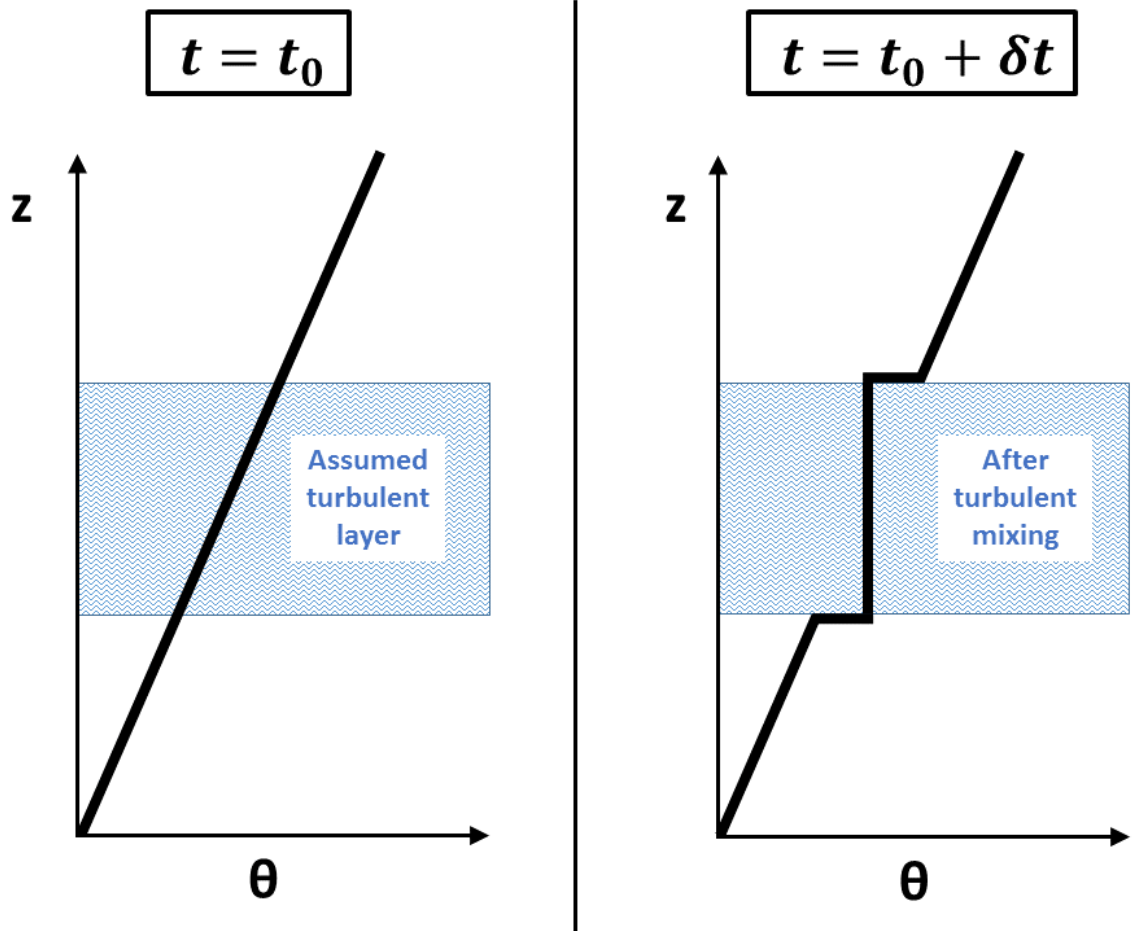


FIG. 10. Schematic diagram of the effect of turbulent mixing on the vertical profile of potential temperature (θ). At the initial time (left panel), potential temperature is assumed to increase with height at a constant rate (thick black line). The imposition of turbulence within a portion of the layer (blue hatching) adjusts the potential temperature profile toward the mean initial value of that layer. After a period of mixing (right panel) the potential temperature in the mixed layer does not vary with height, but just above and just below the mixed layer, it rapidly increases with height.

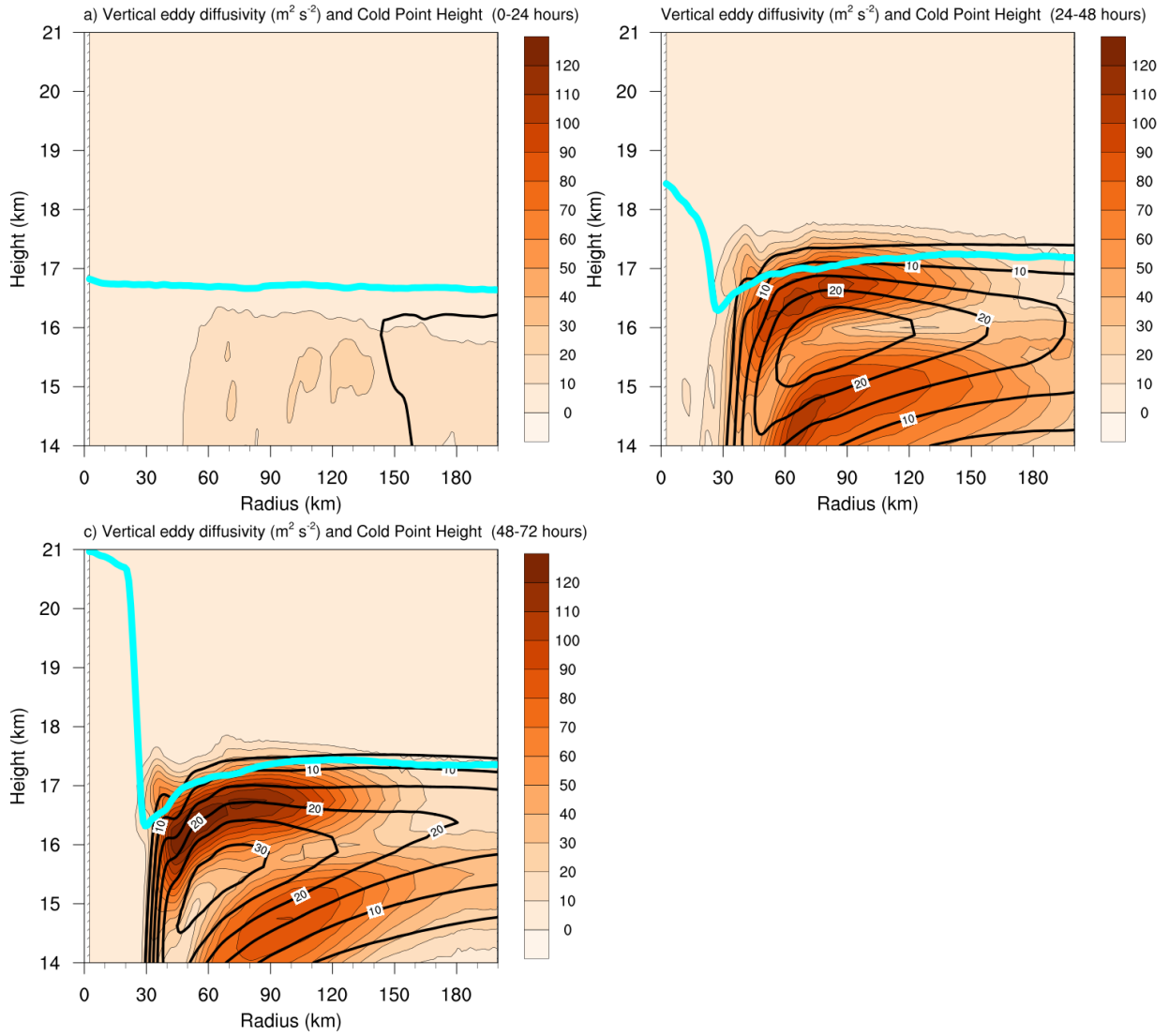
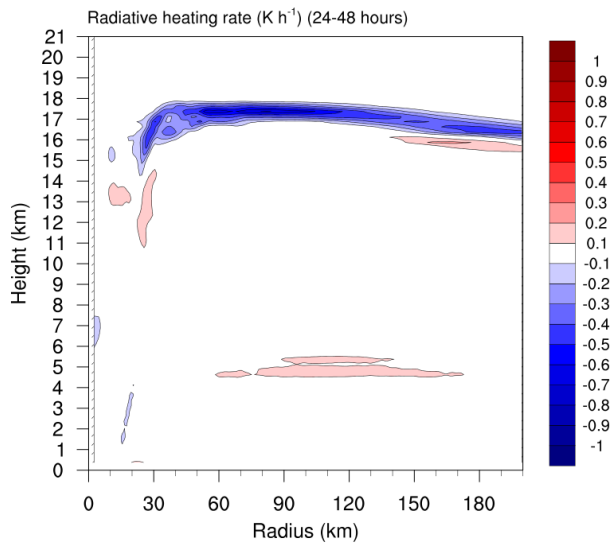
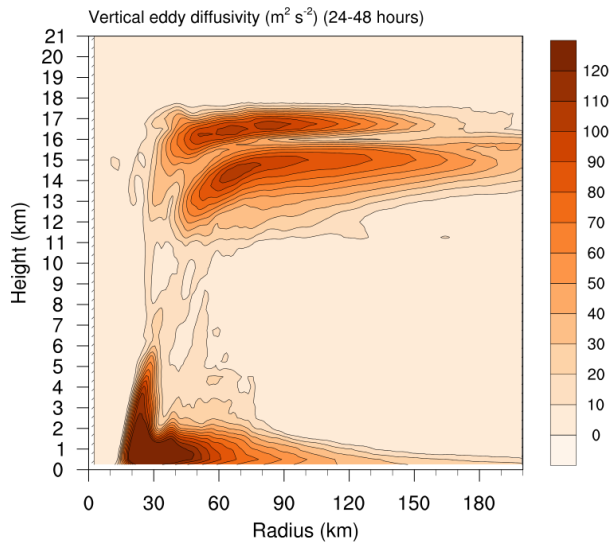
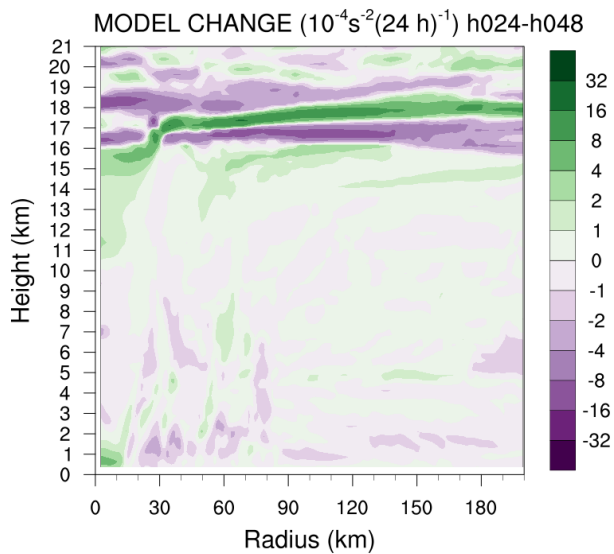


FIG. 11. Vertical eddy diffusivity ($\text{m}^2 \text{s}^{-2}$; filled contours), cold-point tropopause height (cyan lines), and radial velocity (m s^{-1} ; thick black lines) averaged over (a) 0-24 hours, (b) 24-48 hours, and (c) 48-72 hours.



550 FIG. 12. (Top panel) Change in N^2 over the 24-48-hour period ($10^{-4} \text{ s}^{-2} (24 \text{ h})^{-1}$) directly output by the model
551 for the 0-21-km layer. (Middle panel) Vertical eddy diffusivity ($\text{m}^2 \text{ s}^{-2}$) averaged over the same time period.
552 (Bottom panel) Radiative heating rate (K h^{-1}) averaged over the same time period.